Journal of Materials Chemistry A

PAPER

Check for updates

Cite this: J. Mater. Chem. A, 2019, 7, 3971

Linear-like lead-free relaxor antiferroelectric $(Bi_{0.5}Na_{0.5})TiO_3$–$NaNbO_3$ with giant energy-storage density/efficiency and super stability against temperature and frequency

He Qi and Ruzhong Zuo *

A novel lead-free polar dielectric ceramic with linear-like polarization responses was found in $(1-x)(Bi_{0.5}Na_{0.5})TiO_3$–$xNaNbO_3$ ($(1-x)$BNT–xNN) solid solutions, exhibiting giant energy storage density/efficiency and super stability against temperature and frequency. High-resolution transmission electron microscopy, Raman scattering and Rietveld refinements of X-ray diffraction data suggest that these property characteristics can be derived from temperature and electric field insensitive large permittivity as a result of relaxor antiferroelectricity (AFE) with polar nanoregions. Additionally, this feature intrinsically requires a high driving field for AFE to ferroelectric (FE) phase transitions due to large random fields. Measurements of temperature-dependent permittivity and polarization *versus* electric field hysteresis loops indicate that the high-temperature AFE *P4bm* phase in BNT was gradually stabilized close to room temperature, accompanying a phase transition from relaxor rhombohedral FEs to relaxor tetragonal AFEs approximately at $x = 0.15$–0.2. A record high of recoverable energy-storage density $W \sim 7.02$ J cm^{-3} as well as a high efficiency $\eta \sim 85\%$ was simultaneously achieved in the $x = 0.22$ bulk ceramic, which challenges the existing fact that W and η must be seriously compromised. Furthermore, desirable W (>3.5 J cm^{-3}) and η (>88%) with a variation of less than 10% can be accordingly obtained in the temperature range of 25–250 °C and frequency range of 0.1–100 Hz. These excellent energy-storage properties would make BNT-based lead-free AFE ceramic systems a potential candidate for application in pulsed power systems.

Received 19th December 2018
Accepted 18th January 2019

DOI: 10.1039/c8ta12232f

rsc.li/materials-a

1. Introduction

Dielectric capacitors have been playing indispensable roles in modern electronic and electrical devices owing to their high power density and fast charge/discharge rates.[1–3] The recoverable energy-storage density W and efficiency η of a capacitor can be determined according to a polarization–electric field (P–E) loop during a charge–discharge period using the following formula: $W = \int_{P_r}^{P_{max}} E\mathrm{d}P$, $W_{loss} = \int P\mathrm{d}E$, and $\eta = W/(W + W_{loss})$, where P_{max} is the saturated polarization, P_r is the remanent polarization, and W_{loss} is the area of hysteresis loop.[4–6] Accordingly, high electric breakdown field (E_B), large P_{max} and low P_r have to be satisfied simultaneously for a dielectric material with obviously enhanced energy-storage properties.[7–17] From this point of view, antiferroelectric (AFE) ceramics and relaxor ferroelectric (FE) ceramics might have large potential against purely linear nonpolar dielectrics.[4–8,18] The latter was believed to have the highest η values but rather low W values as a result of the polarization extension effect solely and low dielectric permittivity ε_r (see Fig. 1a). By comparison, relaxor FE ceramics generally have higher η values as a result of a low-hysteresis polarization response, but limited W values based on lower P_{max} values originating from insufficient polarization switching caused by large random fields or reduced dielectric breakdown strength caused by high ε_r (see Fig. 1a).[19–22] The maximum W values in bulk ceramics have been so far reported in AFE ceramics.[7] W values of up to 6.4 J cm^{-3} and 4.4 J cm^{-3} were achieved in spark plasma sintered (Pb,La)(Zr,Ti)O_3 and $AgNbO_3$ (AN)-based AFE ceramics, respectively,[7,8] owing to the reversible first-order AFE–FE phase transition. However, one obvious drawback of normal AFEs is the high polarization hysteresis loss formed between the charge and discharge process, as shown in Fig. 1a. It is thus essential for an AFE energy-storage ceramic to effectively reduce the field value difference between forward and backward phase switching and simultaneously enhance its driving electric field (E_{dri}) for the AFE to FE phase transition and E_B values as well.[8]

It has been indicated recently that the combination of relaxor features and the AFE phase could effectively optimize

Institute of Electro Ceramics & Devices, School of Materials Science and Engineering, Hefei University of Technology, Hefei, 230009, P. R. China. E-mail: piezolab@hfut.edu.cn; Fax: +86-551-62905285; Tel: +86-551-62905285

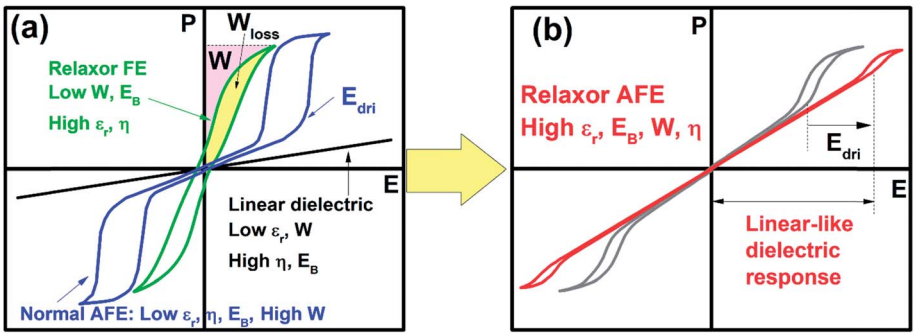

Fig. 1 Schematic diagram of energy storage properties for various types of dielectric ceramics: (a) the *P*–*E* loops for purely linear nonpolar dielectric, relaxor FE and normal AFE ceramics, and (b) the *P*–*E* loops expected for a relaxor AFE ceramic.

both forward and backward switching processes during field induced AFE–FE phase transition,[23,24] generating a relatively high η value but maintaining a high W value at the same time by reducing the loop area. However, the hysteresis process still exists during charging and discharging, such that the η values must be sacrificed, only if the AFE to FE phase transition is completely involved under a sufficiently high external field (see grey curve in Fig. 1b). However, it would be also desirable for an AFE phase if its driving field E_{dri} is so high that the linear-like dielectric response part will dominate the charge–discharge process as the applied field is only close to the E_{dri} value, as shown in red in Fig. 1b. The potential in this case against a purely linear nonpolar dielectric will be reflected by its high dielectric response from antiparallel spontaneous polarization vectors. Moreover, it would also endure a higher electric field magnitude than normal AFE ceramics in which an extremely high phase switching current involved during loading would tend to electrically breakdown the sample.

The high-temperature relaxor phase in $(Bi_{0.5}Na_{0.5})TiO_3$ (BNT) between 200 °C and 320 °C was reported to have an AFE *P4bm* structure, which is distorted from a cubic phase by in-phase rotations of TiO_6 octahedra about the *c* axis, as well as by antiparallel displacement of the cations along the polar *c* axis.[25–27] In addition, BNT-based lead-free perovskites might have obvious advantages in energy-storage capacitors owing to their large spontaneous polarization of over 40 μC cm^{-2}.[28,29] The energy-storage density can be further increased up to $W = 9.5$ J cm^{-3} as a multilayer structure with a single-layer thickness of ~20 μm was applied, and even $W > 50$ J cm^{-3} as a thick film of ~1 μm was fabricated by a sol–gel method.[24,30,31] Unfortunately, the maximum W value achieved in BNT-based bulk ceramics was reported so far to be still less than 3 J cm^{-3}.[12,22,32–34] $NaNbO_3$ (NN) was believed to be an AFE orthorhombic phase at room temperature (RT) and has a lower tolerance factor than BNT,[35] being expected to stabilize the high-temperature AFE phase of BNT. In this work, BNT–NN binary solid solution ceramics were found to exhibit an extremely-stable giant energy storage density/efficiency within a wide temperature and frequency range, and realize an excellent balance among W, η and their stability. High-resolution transmission electron microscopy (HR-TEM), Rietveld refinements of X-ray diffraction data (XRD), measurements of temperature-dependent permittivity and *P*–*E* hysteresis loops were adopted to explore the relevant physical mechanisms.

2. Experimental section

$(1 - x)$BNT–xNN (x = 0–0.5 in molar) and $BaCu(B_2O_5)$ (BCB) were prepared using analytical reagents Na_2CO_3, Nb_2O_5, Bi_2O_3, TiO_2, $Ba(OH)_2 \cdot 8H_2O$ (≥99%), CuO (≥99%) and H_3BO_3 *via* a standard solid-state reaction method. The powders were mixed thoroughly in ethanol using zirconia balls for 12 hours in stoichiometric amounts. Then, the dried $(1 - x)$BNT–xNN and BCB powders were calcined at 850 °C and 810 °C in air for 5 h, respectively. 2 wt% BCB powder was added into part of the calcined 0.78BNT–0.22NN powder in order to optimize its sintering behavior. The powder was ball-milled again for 24 hours, and then pressed into disk samples with a diameter of 10 mm under 100 MPa using polyvinyl alcohol as the binder. The disk samples were sintered at 1000–1250 °C for 2 hours in air after burning out the binder at 550 °C for 4 hours. The sintered disks were well polished into a thickness of 0.25–0.3 mm between two parallel faces. Silver electrodes were pasted and then fired on both sides of the samples at 550 °C for 30 min.

The temperature dependent *P*–*E* hysteresis loops were measured by using a ferroelectric testing system (Precision Multiferroic, Radiant Technologies Inc., Albuquerque, NM) connected to a high-temperature probing stage (HFS600E-PB2, Linkam Scientific Instruments, Tadworth, UK). Dielectric properties as a function of temperature and frequency were measured using an LCR meter (Agilent E4980A, Santa Clara, CA). XRD measurements under different temperatures were performed with Cu Kα radiation at an acceleration condition of 40 kV and 30 mA (D/Max2500V; Rigaku, Tokyo, Japan). Rietveld refinements were performed by using the program GSAS. The grain morphology was observed by using a field-emission scanning electron microscope (FE-SEM, SU8020, JEOL, Tokyo, Japan). Before the SEM observation, the samples were polished and thermally etched at ~1000 °C for 30 min. The domain morphology observation, selected area electron diffraction (SAED) and HR atomic imaging were performed on a field emission transmission electron microscope (FE-TEM, JEM-2100F, JEOL, Japan) operated at 200 kV. Temperature dependent Raman spectra were collected on well-polished pellets by

532 nm excitation using a Raman spectrometer (LabRam HR Evolution, HORIBA JOBIN YVON, Longjumeau Cedex, France).

3. Results and discussion

Fig. 2 shows the evolution of dielectric, ferroelectric and energy-storage properties of $(1-x)$BNT–xNN ceramics sintered at optimum temperatures. An obvious dielectric anomaly corresponding to the FE rhombohedral (R) to AFE tetragonal (T) phase transition can be found at $T_{RT} \sim 250$ °C for pure BNT ceramics. By substituting NN for BNT, T_{RT} decreases monotonously and drops below RT starting at $x = 0.2$. Accompanied by the disappearance of T_{RT}, the sample starts to possess an AFE T phase at RT with a nearly temperature-stable permittivity *vs.* temperature curve. Moreover, an obviously enhanced dielectric relaxation feature can be detected owing to the addition of NN into BNT, as evidenced by the decreased temperature corresponding to the electric field induced FE to ergodic relaxor phase transition temperature (T'_{FR}) during heating for poled samples, as shown in the inset of Fig. 2b. According to the dielectric properties, the phase diagram of $(1-x)$BNT–xNN ceramics was plotted, as shown in Fig. 2b. The phase structure at RT changes from a nonergodic relaxor FE R (R_{NR}) phase to an ergodic relaxor FE R (R_{ER}) phase, and then to a relaxor AFE T (T_{AFE}) phase with increasing NN content. As a result, *P*–*E* loops gradually change from a square shape ($0 \le x \le 0.06$) to a pinched shape ($0.1 \le x \le 0.15$) and finally to a nearly linear shape ($x \ge 0.2$), leading to decreased P_{max} and P_r values, but improved energy storage properties, as demonstrated in Fig. 2d and e, respectively. It can be seen from Fig. 2d that $\Delta P\,(=P_{max}-P_r)$ can reach its maximum approximately at $x = 0.15$. Therefore, the W values first increase with increasing NN content and then reach the maximum value (0.98 J cm^{-3} as the applied field is 10 kV mm^{-1}) at $x = 0.15$ as well. However, the $x = 0.15$ sample still exhibits a slightly hysteretic *P*–*E* loop, such that its storage efficiency η is not high enough. With further increasing NN content, the η value rapidly increases and almost arrives at a plateau of ~94–97% for samples with $x \ge 0.22$. Compared to samples with $x < 0.2$, samples with $x \ge 0.2$ exhibit a nearly identical change tendency of W values to that of dielectric permittivity, as shown in Fig. 2f. This is because a nearly hysteresis-free linear-like dielectric response was involved as the applied electric field is lower than E_{dri} for AFE ceramics. Both enhanced AFE stability and increased relaxation behavior due to the substitution of NN for BNT were believed to help increase the driving field for phase switching. A slight *P*–*E* hysteresis observed in $x = 0.15$ and 0.2 samples should be due to the fact that their corresponding E_{dri} might be not much higher than the applied electric field of 10 kV mm^{-1}. In addition, from the permittivity *vs.* temperature curves in Fig. 2a, one can easily calculate the permittivity variation with respect to the respective RT value $((\varepsilon_r - \varepsilon_{RT})/\varepsilon_{RT})$ as a function of measuring temperature. As the permittivity variation is within ±10%, a plot of the upper limit temperature $(T_{\pm 10\%})$ against the NN content x can be drawn, as shown in Fig. 2f. It can be seen that the $x = 0.22$ sample has a relatively high $\varepsilon_r \sim 1500$ at RT and a temperature insensitive permittivity (less than ±10%) up to a temperature of $T_{\pm 10\%} \sim 390$ °C. With further increasing x above 0.22, both RT, ε_r and the corresponding $T_{\pm 10\%}$ obviously decrease. The permittivity values for these samples with $x \ge 0.22$ are much larger than those of other thermally-stable linear dielectrics (such as glasses and glass-ceramics)[6,16,17] owing to the existence of the local AFE ordering. As a result, the linear-like dielectric ceramic of $x = 0.22$ should show large potential in energy-storage applications if its breakdown strength value can be enhanced.

P–*E* hysteresis loops measured at 10 Hz under different electric fields for BCB doped $x = 0.22$ ceramic are shown in Fig. 3a. A nearly linear *P*–*E* loop can be seen during electric cycling when the applied electric field is lower than 25 kV mm^{-1}, as indicated by a nearly unchanged current density (Fig. 3b). This indicates that no obvious domain switching or phase transition is involved during loading. During this field range, the AFE polar nanoregions (PNRs) grow into micro-domains and orient along the electric field direction, behaving like FE PNRs in response to the external fields.[36] As the applied

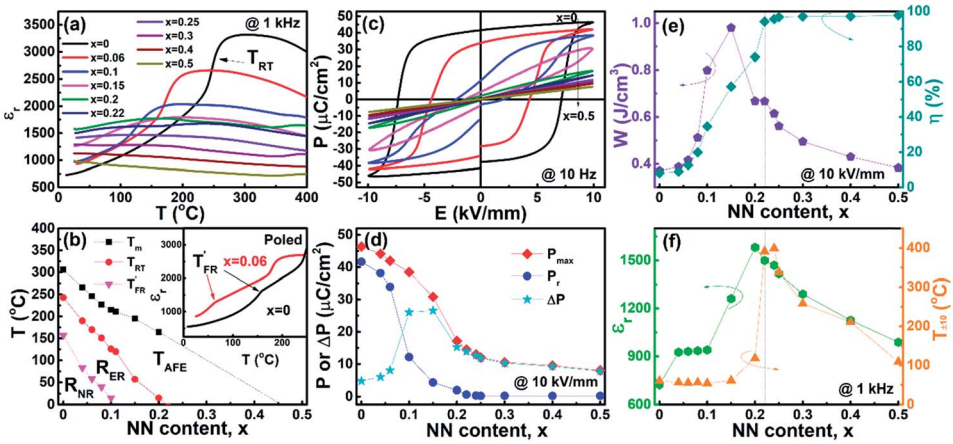

Fig. 2 (a) Temperature dependent dielectric permittivity ε_r for $(1-x)$BNT–xNN ceramics, (b) the phase diagram of $(1-x)$ the BNT–xNN binary system, (c) *P*–*E* loops of $(1-x)$BNT–xNN ceramics, and the evolution of (d) P_{max}, P_r and ΔP, (e) W and η values, and (f) RT ε_r and $T_{\pm 10\%}$ with changing NN content. The inset shows the temperature dependence of ε_r for the poled samples with $x = 0$ and $x = 0.06$; $T_{\pm 10\%}$ stands for the upper-limit temperature until which the variation of ε_r with respect to its RT value is within ±10%.

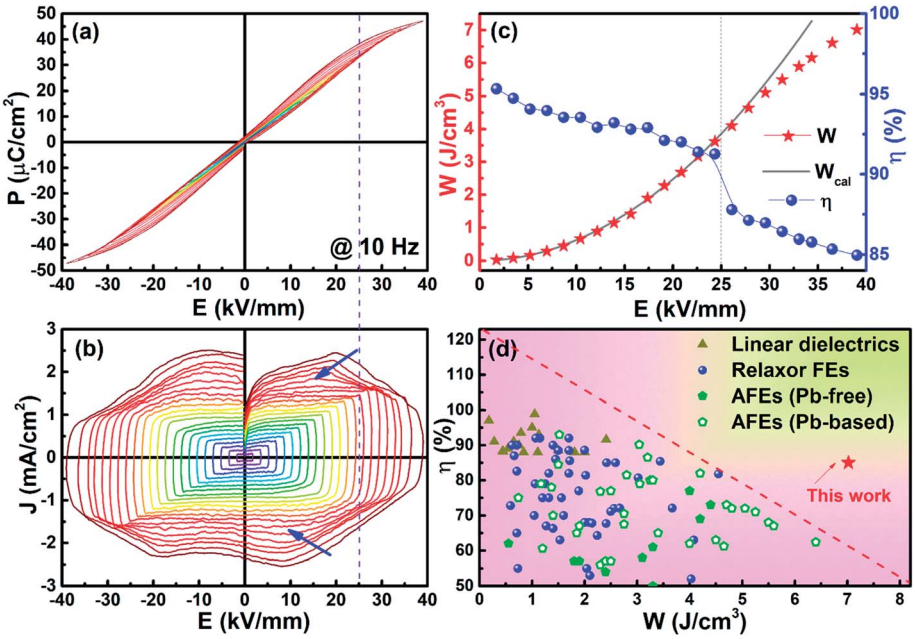

Fig. 3 (a) RT P–E loops and (b) the corresponding polarization current density *vs.* electric field (J–E) curves of the BCB doped $x = 0.22$ ceramic under different electric fields at a fixed frequency of 10 Hz, (c) the variation of W, W_{cal} and η values of the BCB doped $x = 0.22$ ceramic with the magnitude of the applied electric field, and (d) a comparison of W and η values among recently reported bulk ceramics.[4–17,19–23,32–34,37–40]

electric field is more than 25 kV mm^{-1}, a detectable polarization current peak (as marked by arrows in Fig. 3b) can be more and more clearly seen, and is accompanied by forming a more hysteretic P–E loop, suggesting that oriented AFE micro-domains would gradually transform into textured long-range FE orders under a high enough electric field through phase switching. This above process is characterized by the nonlinearity and hysteresis of the polarization response. Thus, the calculated W value should approximately obey the relationship of $W_{cal} = \varepsilon_o\varepsilon_r E^2/2$ for the linear part of P–E loops, as reflected by the parabolic relationship of W and E in the electric field range of 0–25 kV mm^{-1} in Fig. 3c. The obvious deviation of the W_{cal} value from the real W value indicates that permittivity is obviously electric field dependent as E is above 25 kV mm^{-1}. A rapid decline of η values can be observed concurrently owing to the increased polarization hysteresis. Nevertheless, a record high of $W\sim$7.02 J cm^{-3} and a desirable energy efficiency of $\eta\sim$ 85% can be obtained simultaneously under an external field of ~39 kV mm^{-1}, where a long-range FE order has not yet been established completely (see Fig. 3a).

A comparison of W and η values of recently reported bulk dielectric ceramics is shown in Fig. 3d.[4–17,19–23,32–34,37–40] It can be clearly seen that a relationship of mutual constraint exists between W and η values for a couple of dielectrics. Both of them are usually located under the diagonal line of Fig. 3d for most of currently reported bulk dielectric ceramics. The existence of such a bottleneck in the field of dielectric energy storage is basically due to the fact that high ε_r is not beneficial to E_B.[41] The solution to this issue is clearly of significance for industrial applications. The W values of relaxor FE and purely linear nonpolar dielectric ceramics are limited to the low E_B value and low ε_r value, respectively, even though their η values are relatively high. A large W could be achieved in normal AFE ceramics, however, their η values are relatively low owing to the obvious hysteresis from the reversible AFE–FE phase transition. By comparison, the relaxor AFE BNT–NN ceramic with $x = 0.22$ exhibits a huge advantage over others, reaching an excellent balance between W and η values as the applied field is just close to the E_{dri} value.

Fig. 4a and b show P–E loops of the $x = 0.22$ ceramic measured at different temperatures and frequencies under an external electric field of 25 kV mm^{-1}, where a linear-like low-hysteresis dielectric response is involved as mentioned above. Only a slight variation of P_{max}, P_r and the hysteresis degree with changing temperature and frequency can be observed probably because the applied electric field is not much higher than both the random electric field and the E_{dri}. The growth and orientation of AFE PNRs in response to electric fields should dominate the polarization response process, so that the P–E loops are not sensitive to the variation of temperature and frequency, leading to frequency and temperature independent W and η values, as shown in Fig. 4c. On the one hand, the response of AFE PNRs to electric fields for the $x = 0.22$ ceramic is very fast within the measuring frequency and temperature range owing to large random electric fields. On the other hand, the nearly linear polarization response in Fig. 4a indicates that dielectric permittivity ε_r is independent of the magnitude of the applied electric field. As a result, the temperature and frequency dependence of W values should be mainly controlled by the variation of ε_r, as shown in Fig. 4d. The ε_r measured from 0.1 Hz to 1 MHz can be kept within a small fluctuation of ±10% in a wide temperature range of 25–250 °C. Nevertheless, a slight contribution from the AFE domain wall motion, not from domain orientation approximately at 25 kV mm^{-1} should be

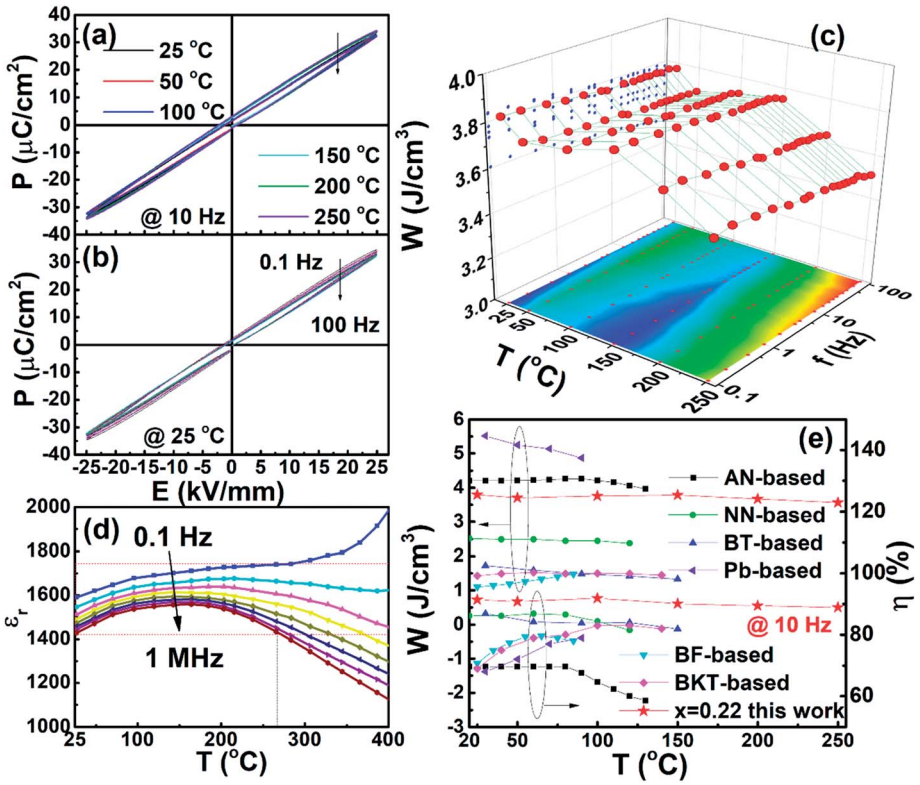

Fig. 4 (a) Temperature and (b) frequency dependent *P*–*E* hysteresis loops of the BCB doped $x = 0.22$ ceramic under an electric field of 25 kV mm^{-1}, (c) the *W* value of the BCB doped $x = 0.22$ ceramic derived from *P*–*E* loops as a function of temperature and frequency, (d) the variation of dielectric permittivity ε_r measured at various frequencies against temperature for BCB doped $x = 0.22$ ceramic, and (e) the variation of *W* and η as a function of temperature for a few typical energy-storage bulk ceramics.[10,13,15,20,39,40]

responsible for the small polarization hysteresis observed in Fig. 4a, leading to a η value of ~90%, not 100%. A slightly reduced η value at a higher temperature might be ascribed to the contribution of the conduction loss during test.[42] Fig. 4e demonstrates the comparison of temperature-dependent *W* and η values between the $x = 0.22$ ceramic in the current work and a few other bulk Pb-free and Pb-based ceramics ($(Bi_{0.5}K_{0.5})TiO_3$: BKT, $BaTiO_3$: BT and $BiFeO_3$: BF).[10,13,15,20,39,40] It can be seen that the $x = 0.22$ ceramic exhibits an obvious advantage in both *W* and η values against almost all other lead-free ceramics, showing not only much larger energy storage properties (*W*: 3.51–3.85 J cm^{-3} and η: 88–90%) but also much better stability in the temperature range of 25–250 °C and frequency range of 0.1–100 Hz. Even though the *W* value of AN-based and Pb-based AFE ceramics is comparable with that of the $x = 0.22$ ceramic, a much smaller η value was reported as a result of the hysteretic AFE–FE phase transition. This result means that a linear-like dielectric response in a relaxor AFE ceramic below the critical field for the complete AFE–FE phase transition would help realize relatively desirable balance between *W* and η, compared with other dielectrics such as linear nonpolar dielectrics, relaxor FEs and normal AFE ceramics.

To better understand the excellent energy storage performances of the BCB doped $x = 0.22$ ceramic, SEM photos were taken on the well-polished and thermally etched surface of the $x = 0.22$ (sintered at 1160 °C) and BCB doped $x = 0.22$ (sintered at 1020 °C) ceramics, as shown in Fig. 5a and b. It can be found that the average grain size decreases significantly after the addition of BCB, as statistically analyzed in the inset of Fig. 5a and b. The BCB doped $x = 0.22$ sample exhibits a dense and uniform microstructure with an average grain size of ~0.5 mm and a high relative density of more than 98% at a relatively low sintering temperature by means of liquid-phase sintering as observed at grain boundaries and triple joints, leading to the enhancement of the breakdown field. For pure BNT ceramics ($x = 0$), an irregular or dirty domain morphology together with 1/2{*ooo*} superlattice reflections (*o* and *e* stand for the odd and even Miller indices, respectively)[43] can be observed in Fig. 5c, suggesting a nonergodic relaxor FE phase with an *R*3*c* space group. The blotchy domain morphology corresponding to the AFE PNRs can be observed on a bright-field image of the BCB doped $x = 0.22$ ceramic, as shown in Fig. 5d. Fig. 5e–h show HR-TEM images of lattice fringes and the SAED patterns along $[111]_C$ and $[001]_C$ for the BCB doped $x = 0.22$ ceramic, indicating the ordered arrangement of atoms and the fine crystalline quality. The SAED patterns indicate the 1/2{*ooe*} superlattice spots as observed along both of the $[111]_C$ and $[001]_C$ axes. Various possibilities of *R*3*c*, *P*4*mm*, *P*4*bm*, and $Pm\bar{3}m$ symmetries might be involved in terms of BNT-based ceramics.[27,44] However, no superlattice spot should be found in both *P*4*mm* and $Pm\bar{3}m$ symmetries. The *R*3*c* symmetry is characterized by the presence of 1/2{*ooo*} and the absence of 1/2{*ooe*} superlattice

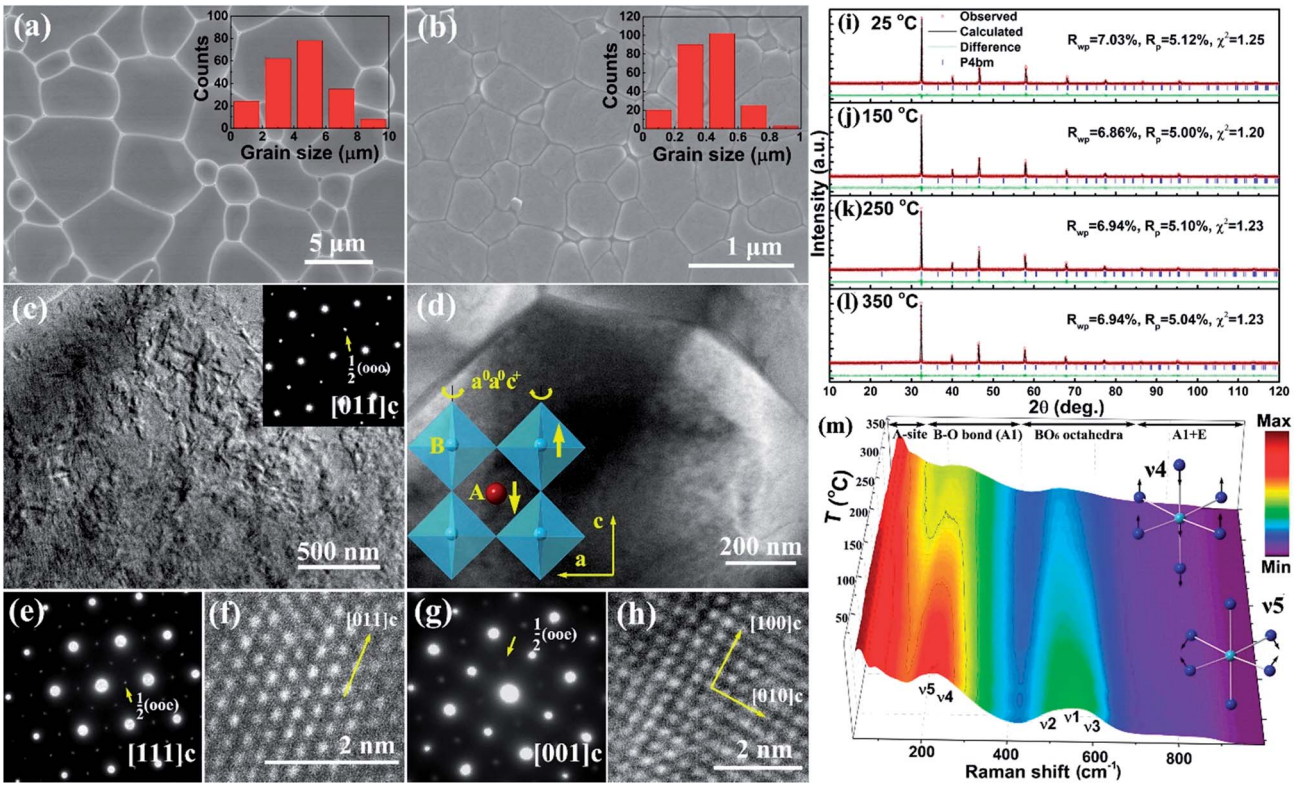

Fig. 5 Grain morphology for the (a) $x = 0.22$ and (b) BCB doped $x = 0.22$ ceramics; (c) bright-field TEM image and the corresponding SAED pattern along $[011]_C$ for the $x = 0$ ceramic at RT, (d) bright-field TEM image, SAED patterns and the HR-TEM images of lattice fringes along (e and f) $[111]_C$ and (g and h) $[001]_C$, respectively, for the BCB doped $x = 0.22$ ceramic at RT; the Rietveld refinement results of XRD patterns for the BCB doped $x = 0.22$ composition measured at (i) 25 °C, (j) 150 °C, (k) 250 °C and (l) 350 °C; (m) Raman spectra of the BCB doped $x = 0.22$ ceramic measured at various temperatures and schematic representations for the ν4 stretching and ν5 bending modes. The insets of (a) and (b) show the corresponding histograms of the grain size distribution; the inset of (d) is a view of the *P4bm* structure along $[010]_C$, showing the octahedral tilting about the polar *c* axis and the relative cation displacements.

spots, while the *P4bm* phase is featured with the presence of 1/2 {*ooo*} superlattice spots but lack of 1/2{*ooe*} ones. Therefore, the appearance of the 1/2{*ooe*} superlattice spots in the current study suggests a unique structure of the *P4bm* phase with the $a^0a^0c^+$ oxygen octahedron in the studied composition, further confirming an AFE state of the $x = 0.22$ ceramic at RT. In addition, the AFE phase with a *P4bm* space group can also be identified by the Rietveld refinement of full XRD profiles measured at different temperatures, as shown in Fig. 5i–l. The detailed structural parameters and reliability factors at various temperatures are listed in Table 1. The reliability factor of weighted patterns (R_{wp}), the reliability factor of patterns (R_p) and the goodness-of-fit indicator (χ^2) are in the range of 6.86–7.03%, 5.00–5.12% and 1.20–1.25, respectively, indicating that the structural model is valid and the refinement result is reliable. In addition, the splitting of the B–O modes (ν4 and ν5) around 240 cm^{-1} on Raman spectra is preserved in the studied temperature range (Fig. 5m), suggesting a typical T phase character due to the existence of ν4 mode representing the double-degenerate O–B–O stretching vibration.[28] The position of the Raman peaks at around 240 cm^{-1} and 550 cm^{-1} shifts to the lower wavenumber, indicating the weakening of the B–O bonds, which should be related to the loss of hybridization between the empty Ti^{4+}/Nb^{5+} d-orbitals and the oxygen p-orbitals when the dynamics of the PNRs increases. To better understand the structure of the AFE phase, a view of the structure in the $[010]_C$ direction showing the tilt system and relative cation displacements of the *P4bm* phase in the BNT–NN ceramic is shown in the inset of Fig. 5d. The results reveal that the AFE T phase in the $x = 0.22$ ceramic can be maintained from

Table 1 Refined structural parameters by using the Rietveld method for the BCB doped $x = 0.22$ ceramic measured at various temperatures

Temperature (°C)	Space group	Lattice parameters	V (Å^3)	R_{wp} (%)	R_p (%)	χ^2
25	*P4bm*	$a = b = 5.4988(1)$ Å, $c = 3.8939(1)$ Å, $\alpha = \beta = \gamma = 90°$	117.745(9)	7.03	5.12	1.25
150	*P4bm*	$a = b = 5.5049(1)$ Å, $c = 3.9001(1)$ Å, $\alpha = \beta = \gamma = 90°$	118.193(9)	6.86	5.00	1.20
250	*P4bm*	$a = b = 5.5117(1)$ Å, $c = 3.9061(1)$ Å, $\alpha = \beta = \gamma = 90°$	118.669(9)	6.94	5.10	1.23
350	*P4bm*	$a = b = 5.5198(1)$ Å, $c = 3.9116(1)$ Å, $\alpha = \beta = \gamma = 90°$	119.186(9)	6.94	5.04	1.23

RT up to at least 350 °C. These structural features would lay a solid foundation for achieving excellent energy storage properties by taking advantage of the hysteresis-free linear-like polarization response in a relaxor AFE BNT–NN lead-free ceramic.

4. Conclusions

A linear-like polar ceramic dielectric with a lead-free composition of $(1-x)$BNT–xNN was found to exhibit excellent energy-storage properties and super stability against temperature and frequency. The achievement of these properties was believed to originate from the relaxor AFE *P4bm* phase stabilized through the substitution of NN for BNT, as evidenced by HR-TEM, Raman spectrum and Rietveld refinements of XRD data. Large random electric fields offer the AFE PNRs the possibility of temperature and electric field insensitive polarization responses as a relatively high external electric field is loaded. Accordingly, a record high of $W \sim 7.02$ J cm^{-3} and a large η of $\sim 85\%$ can be simultaneously achieved in the $x = 0.22$ ceramic as an electric field of 39 kV mm^{-1} was applied, showing huge advantages in overall energy-storage properties over various kinds of bulk dielectric ceramics reported so far, especially linear nonpolar dielectrics or normal AFE ceramics. Furthermore, the desirable W (>3.5 J cm^{-3}) and η (>88%) values with a variation of less than 10% can be also obtained in a wide temperature range from 25 to 250 °C and in a frequency range of 0.1–100 Hz because of the stable AFE state and the fast polarization response under the application of an electric field of 25 kV mm^{-1}. These results demonstrate that BNT–NN relaxor AFE ceramics would be a potential lead-free bulk dielectric material for future pulsed power capacitor applications.

Conflicts of interest

There are no conflicts of interest to declare.

Acknowledgements

This work was supported by the National Natural Science Foundation of China (Grants No. 51472069) and China Postdoctoral Science Foundation (Grants No. 2018M642998).

References

1 B. J. Chu, X. Zhou, K. L. Ren, B. Neese, M. R. Lin, Q. Wang, F. Bauer and Q. M. Zhang, *Science*, 2006, **313**, 334–336.
2 S. Wu, W. P. Li, M. R. Lin, Q. Burlingame, Q. Chen, A. Payzant, K. Xiao and Q. M. Zhang, *Adv. Mater.*, 2013, **25**, 1734–1738.
3 G. R. Love, *J. Am. Ceram. Soc.*, 1990, **73**, 323–328.
4 X. H. Hao, *J. Adv. Dielectr.*, 2013, **3**, 1330001.
5 A. Chauhan, S. Patel, R. Vaish and C. R. Bowen, *Materials*, 2015, **8**, 8009–8031.
6 Z. H. Yao, Z. Song, H. Hao, Z. Y. Yu, M. H. Cao, S. J. Zhang, M. T. Lanagan and H. X. Liu, *Adv. Mater.*, 2017, **29**, 1601727.
7 L. Zhang, S. L. Jiang, B. Y. Fan and G. Z. Zhang, *J. Alloys Compd.*, 2015, **622**, 162–165.
8 J. Gao, Y. C. Zhang, L. Zhao, K. Y. Lee, Q. Liu, A. Studer, M. Hinterstein, S. J. Zhang and J. F. Li, *J. Mater. Chem. A*, 2019, **7**, 2225–2232.
9 T. Q. Shao, H. L. Du, H. Ma, S. B. Qu, J. Wang, J. F. Wang, X. Y. Wei and Z. Xu, *J. Mater. Chem. A*, 2017, **5**, 554–563.
10 M. X. Zhou, R. L. Liang, Z. Y. Zhou and X. L. Dong, *J. Mater. Chem. A*, 2018, **6**, 17896–17904.
11 W. Huang, Y. Chen, X. Li, G. S. Wang, N. T. Liu, S. Li, M. X. Zhou and X. L. Dong, *Appl. Phys. Lett.*, 2018, **113**, 203902.
12 J. Yin, Y. X. Zhang, X. Lv and J. G. Wu, *J. Mater. Chem. A*, 2018, **6**, 9823–9832.
13 F. Li, T. Jiang, J. W. Zhai, B. Shen and H. R. Zeng, *J. Mater. Chem. C*, 2018, **6**, 7976–7981.
14 H. B. Yang, F. Yan, Y. Lin and T. Wang, *Appl. Phys. Lett.*, 2017, **111**, 253903.
15 N. T. Liu, R. L. Liang, Z. Y. Zhou and X. L. Dong, *J. Mater. Chem. C*, 2018, **6**, 10211–10217.
16 S. M. Xiu, S. Xiao, W. Q. Zhang, S. X. Xue, B. Shen and J. W. Zhai, *J. Alloys Compd.*, 2016, **670**, 217–221.
17 C. Davis III, A. L. Pertuit and J. C. Nino, *J. Am. Ceram. Soc.*, 2017, **100**, 65–73.
18 X. H. Hao, J. W. Zhai, L. B. Kong and Z. K. Xu, *Prog. Mater. Sci.*, 2014, **63**, 1–57.
19 Z. B. Shen, X. H. Wang, B. C. Luo and L. T. Li, *J. Mater. Chem. A*, 2015, **3**, 18146–18153.
20 Q. B. Yuan, F. Z. Yao, Y. F. Wang, R. Ma and H. Wang, *J. Mater. Chem. C*, 2017, **5**, 9552–9558.
21 R. Z. Zuo, H. Qi, J. Fu, J. F. Li, M. Shi and Y. D. Xu, *Appl. Phys. Lett.*, 2016, **108**, 232904.
22 R. A. Malik, A. Hussain, M. Acosta, J. Daniels, H.-S. Han, M.-H. Kim and J.-S. Lee, *J. Eur. Ceram. Soc.*, 2018, **38**, 2511–2519.
23 H. R. Jo and C. S. Lynch, *J. Appl. Phys.*, 2016, **119**, 024104.
24 J. L. Li, F. Li, Z. Xu and S. J. Zhang, *Adv. Mater.*, 2018, **30**, 1802155.
25 V. Dorcet, G. Trolliard and P. Boullay, *J. Magn. Magn. Mater.*, 2009, **321**, 1758–1761.
26 G. O. Jones and P. A. Thomas, *Acta Crystallogr., Sect. B: Struct. Sci.*, 2002, **58**, 168–178.
27 C. Ma, X. Tan, E. Dul'kin and M. Roth, *J. Appl. Phys.*, 2010, **108**, 104105.
28 D. Schütz, M. Deluca, W. Krauss, A. Feteira, T. Jackson and K. Reichmann, *Adv. Funct. Mater.*, 2012, **22**, 2285–2294.
29 S. T. Zhang, A. B. Kounga, W. Jo, C. Jamin, K. Seifert, T. Granzow, J. Rödel and D. Damjanovic, *Adv. Mater.*, 2009, **21**, 4716–4720.
30 N. N. Sun, Y. Li, Q. W. Zhang and X. H. Hao, *J. Mater. Chem. C*, 2018, **6**, 10693–10703.
31 J. H. Wang, Y. Li, N. N. Sun, J. H. Du, Q. W. Zhang and X. H. Hao, *J. Eur. Ceram. Soc.*, 2019, **39**, 255–263.
32 P. Chen and B. J. Chu, *J. Eur. Ceram. Soc.*, 2016, **36**, 81–88.
33 Q. Xu, T. M. Li, H. Hao, S. J. Zhang, Z. J. Wang, M. H. Cao, Z. H. Yao and H. X. Liu, *J. Eur. Ceram. Soc.*, 2015, **35**, 545–553.
34 A. Mishra, B. Majumdar and R. Ranjan, *J. Eur. Ceram. Soc.*, 2017, **37**, 2379–2384.

35 S. K. Mishra, N. Choudhury, S. L. Chaplot, P. S. R. Krishna and R. Mittal, *Phys. Rev. B: Condens. Matter Mater. Phys.*, 2007, **76**, 024110.
36 W. L. Zhao, R. Z. Zuo, J. Fu, X. H. Wang, L. T. Li, H. Qi and D. G. Zheng, *J. Eur. Ceram. Soc.*, 2016, **36**, 2453–2460.
37 D. G. Zheng and R. Z. Zuo, *J. Eur. Ceram. Soc.*, 2017, **37**, 413–418.
38 Y. Tian, L. Jin, H. F. Zhang, Z. Xu, X. Y. Wei, E. D. Politova, S. Y. Stefanovich, N. V. Tarakina, I. Abrahams and H. X. Yan, *J. Mater. Chem. A*, 2016, **4**, 17279–17287.
39 Q. F. Zhang, H. F. Tong, J. Chen, Y. M. Lu, T. Q. Yang, X. Yao and Y. B. He, *Appl. Phys. Lett.*, 2016, **109**, 262901.
40 L. Zhao, Q. Liu, J. Gao, S. J. Zhang and J. F. Li, *Adv. Mater.*, 2017, **29**, 1701824.
41 L. T. Yang, X. Kong, F. Li, H. Hao, Z. X. Cheng, H. X. Liu, J. F. Li and S. J. Zhang, *Prog. Mater. Sci.*, 2019, **102**, 72–108.
42 Q. Chen, Y. Wang, X. Zhou, Q. M. Zhang and S. H. Zhang, *Appl. Phys. Lett.*, 2008, **92**, 142909.
43 A. M. Glazer, *Acta Crystallogr., Sect. A: Cryst. Phys., Diffr., Theor. Gen. Crystallogr.*, 1975, **31**, 756–762.
44 V. Dorcet and G. Trolliard, *Acta Mater.*, 2008, **56**, 1753–1761.